J Mol Model (2007) 13:1109–1121
DOI 10.1007/s00894-007-0235-2

ORIGINAL PAPER

Hybrid density functional theory with a specific reaction parameter: hydrogen abstraction reaction of difluoromethane by the hydroxyl radical

Titus V. Albu · Saravanan Swaminathan

Received: 20 April 2007 / Accepted: 18 July 2007 / Published online: 18 August 2007

Abstract Accurate potential energy surfaces for the OH+$CH_2F_2 \rightarrow H_2O+CHF_2$ reaction are constructed using hybrid and hybrid meta density functional theory methods (mPW1PW91, B1B95, and mPW1B95) with specific reaction parameters in conjunction with the 6–31+G(d,p) basis set. The accuracy of a surface is examined by comparing the calculated rate constants with the experimental ones. The rate constants are calculated over the temperature range 200–1,500 K using variational transition state theory with multidimensional tunneling contributions. The hybrid density functional theory methods with specific-reaction-parameter Hartree-Fock exchange contributions (39.2–41.0% for mPW1PW91, 41.0–42.2% for B1B95, and 44.9–46.3% for mPW1B95, respectively) provide accurate rate constants over an extended temperature range. The classical barrier height for the hydrogen abstraction reaction on these potential energy surfaces is determined to be 5.0–5.3 kcal mol^{-1}, and the best estimate value is 5.14 kcal mol^{-1}.

Keywords Hydrogen abstraction · Difluoromethane · Density functional theory · Barrier height · Rate constant

Electronic supplementary material The online version of this article (doi:10.1007/s00894-007-0235-2) contains supplementary material, which is available to authorized users.

T. V. Albu (✉) · S. Swaminathan
Department of Chemistry, Tennessee Technological University, Box 5055, Cookeville, TN 38505, USA
e-mail: albu@tntech.edu

Introduction

Chlorofluorocarbons are the major source of stratospheric chlorine, which could become active chlorine leading to ozone depletion in the stratosphere [1, 2]. As a result, hydrochlorofluorocarbons and hydrofluorocarbons have been developed as two classes of chlorofluorocarbon substitutes. Hydrochlorofluorocarbons still contain chlorine and can potentially destroy ozone so the chlorine-free compounds are considered better substitutes for chlorofluorocarbons. Hydrofluorocarbons have a wide range of industrial applications in refrigeration, polyurethane foam production, fire suppressants, rocket fuels, etc. The hydrofluorocarbon under consideration in this work is difluoromethane, industrially known as R32.

As a continuation of our previous studies on the important atmospheric reactions of hydrogen abstraction by the hydroxyl radical [3–5], in the present work, we investigate the reaction of hydroxyl radical with a difluoromethane molecule resulting in the hydrogen abstraction and the formation of water:

$$OH + CH_2F_2 \rightarrow H_2O + CHF_2 \quad (1)$$

The rate constants of this reaction have been experimentally determined in a number of studies [6–14]. Several reviews that include data for this reaction and other significant atmospheric reactions are also available [15–17]. For the current investigation, we consider four Arrhenius experimental fits:

$$k = 7.41 \times 10^{-12} \exp(-2100/T) \text{cm}^3 \text{ molecule}^{-1} \text{ s}^{-1} \quad (2)$$

$$k = 4.40 \times 10^{-12} \exp(-1770/T) \text{cm}^3 \text{ molecule}^{-1} \text{ s}^{-1} \quad (3)$$

$$k = 1.57 \times 10^{-12} \exp(-1470/T) \text{cm}^3 \text{ molecule}^{-1} \text{ s}^{-1} \quad (4)$$

$$k = 1.80 \times 10^{-12} \exp(-1552/T) \text{cm}^3 \text{ molecule}^{-1} \text{ s}^{-1} \quad (5)$$

proposed by Clyne and Holt [7] for the temperature range 293–429 K, by Jeong and Kaufman [9] for the temperature range 250–492 K, by Talukdar et al. [11] for the temperature range 220–380 K, and by Hsu and DeMore [13] for the temperature range 297–383 K, respectively.

Several theoretical studies have also focused on the energetics and dynamics of the title reaction [18–28]. Louis et al. [25] calculated the rate constants by means of conventional transition state theory (TST) using the MP2/6–311G(2d,2p) electronic structure method [29] with single-point corrections at PMP4(SDTQ) level of theory [30–32] and tunneling contributions calculated with the Wigner formula [33]. Korchowiec et al. [23] also calculated rate constants; they used modified G2 [34–36] electronic structure theory and conventional TST with the Wigner formula for tunneling contributions. The modified G2 [36] value of the classical barrier height was determined to be 4.0 kcal mol^{-1}. The study of Schwartz el al. [22] also employed TST calculations of the rate constants but with tunneling contributions calculated for one-dimensional Eckart barriers [37]. Gonzalez-Lafont et al. [27] employed dual-level dynamics calculations using variational transition state theory that involve corrections to the energy, based on higher-level calculations [QCISD(T)/6–311++G(2df,p)//QCISD/6–311G(d,p) or CCSD(T)//MP2/cc-pVTZ where Y//Z refers to optimization at level Z with single point energy calculations at higher level Y], along a reaction path determined using a lower level of theory (PM3). These dual-level dynamics methods [38–41] are typically used because the dynamics calculations using only the higher level of theory are computationally prohibited, and those using only the lower level of theory are not reliable.

In the present study, the rate constants for the title reaction are calculated using variational transition state theory with multidimensional tunneling contributions [42–52] (VTST/MT). VTST/MT is a powerful and affordable method for studying chemical reaction dynamics. The accuracy of the level of electronic structure theory used for the potential energy surface (PES) underlying the dynamics typically limits the accuracy of the dynamics results. Hybrid density functional theory (HDFT) methods are excellent candidates for generating accurate PES because they can be easily parameterized and because they are computationally affordable electronic structure methods. Hybrid density functional methods have been shown to predict accurately a wide variety of molecular and dynamics properties such as molecular geometries, atomization energies, barrier heights, intermolecular interactions, etc. [53–56] The procedure used here involves generating hybrid density functionals that provide accurate rate constants in conjunction with direct dynamics calculations using VTST/MT.

In previous studies, we developed hybrid density functionals with a specific reaction parameter [57] (SRP) for the HO+CH_3F and HO+CHF_3 reactions [4, 5], and in the present study we extend this approach to HO+CH_2F_2. (An approach similar to ours was applied by Pu and Truhlar for constructing a potential energy surface for the H+CH_4→ H_2+CH_3 reaction [58].) Three new HDFT-SRP methods (with one parameter each) that provide accurate rate constants over a wide temperature range are proposed. The advantage of these accurate PESs is that the rate constants are obtained on a single-level PES rather than using dual-level dynamics techniques. The approach used here allows for a better description of the stationary point geometry and a more advanced, multidimensional treatment of the tunneling contributions to the calculated rate constants. The procedure is applicable to other hydrogen abstraction reactions from hydrofluorocarbons or other classes of reactions.

Section Computational methods provides an overview of the theory and computational methodology used, section Results presents the results, and section Analysis and discussion gives analyses and discussions. Conclusions and future applications are provided in the final section.

Computational methods

Variational transition state theory with multidimensional tunneling contributions

The rate constants are calculated using variational transition state theory with multidimensional tunneling contributions [42–52]. The transition state can be understood classically as a dividing surface, also called a generalized transition state (GT), in phase space; it divides the space into a reactant region and a product region [49, 51]. The dividing surface is located at the saddle point in conventional transition state theory, while, in variational transition state theory, the position of the dividing surface is optimized so that trajectories originating at reactants and passing through the dividing surface toward the product region will not recross the surface before being thermalized in the product state. The canonical variational-transition-state theory (CVT) rate constant, k^{CVT}, is obtained by maximizing the generalized free energy of activation (at temperature T), ΔG_T^{GT}, as a function of the position of the generalized

transition state along the reaction path. The reaction path is the minimum energy path (MEP) that is defined as the steepest descent path from the saddle point to both the reactant and product sides in the mass weighted (isoinertial) Cartesian coordinate system in which all coordinates are scaled to a common reduced mass μ [59]. The reaction coordinate, s, is defined as the distance along the MEP with the origin located at the saddle point and is positive on the product side and negative on the reactant side. The maximum in ΔG_T^{GT} determines the location along the MEP of the dynamical bottleneck at a certain temperature, $s_*^{\mathrm{CVT}}(T)$. The CVT free energy of activation is obtained as:

$$\Delta G_T^{\mathrm{CVT}} = \max_s \Delta G_T^{\mathrm{GT}}(s) \tag{6}$$

and k^{CVT} is given by:

$$k^{\mathrm{CVT}}(T) = \sigma \frac{k_B T}{h} \exp\left(-\Delta G_T^{\mathrm{CVT}}/RT\right) \tag{7}$$

where σ is the symmetry factor, k_{B} is Boltzmann's constant, h is Planck's constant, and R is the gas constant. At the saddle point (s=0) one obtains the conventional TST rate constant, k^{TST}, and the saddle point free energy of activation $\Delta G_T^{\ddagger}$. Any deviation of k^{CVT} from k^{TST} is called a variational effect. Calculation of the generalized free energy of activation involves calculation of partition functions that are approximated as products of translational, rotational, vibrational, and electronic partition functions. Translational and rotational partition functions were evaluated classically without symmetry numbers whereas the vibrational partition functions were calculated quantum mechanically within the harmonic approximation. Although anharmonicity is known to be important [44, 60, 61], one can assume a certain amount of cancellation between the anharmonic corrections for the reactant and for the generalized transition states [44].

Quantum mechanical effects along the reaction coordinate are included in this study in the form of temperature-dependent transmission coefficients, κ, that primarily account for multidimensional tunneling. Rate constants including tunneling contributions are computed as:

$$k^{\mathrm{CVT/MT}}(T) = \kappa^{\mathrm{MT}}(T) k^{\mathrm{CVT}}(T) \tag{8}$$

where κ^{MT} is the transmission coefficient. The tunneling calculation is based in part on $V_a^{\mathrm{G}}(s)$, which is the vibrationally adiabatic ground-state potential energy curve defined, for nonlinear systems, as:

$$V_a^{\mathrm{G}}(s) = V_{\mathrm{MEP}}(s) + \sum_{m=1}^{3N_{atoms}-7} \frac{\hbar\omega_m(s)}{2} \tag{9}$$

where V_{MEP}(s) is the classical potential energy along the MEP (with its zero of energy at the reactants), $\omega_m(s)$ is the frequency of generalized normal mode m at location s along the MEP, and N_{atoms} is the total number of atoms in the reactive system (seven for the title reaction). In the present study, the multidimensional transmission coefficients were computed using the centrifugal-dominant, small-curvature, semiclassical, adiabatic, ground-state tunneling (called small-curvature tunneling or SCT) approximation [62, 50]. Computations using the one-dimensional zero-curvature tunneling (ZCT) approximation were also carried out.

Hybrid density functional theory methods

All electronic structure theory calculations in this study were carried out using HDFT methods. In an HDFT method, the one-parameter hybrid Fock-Kohn-Sham operator can be written as:

$$F = F^{\mathrm{H}} + XF^{\mathrm{HFE}} + (1-X)\left(F^{\mathrm{SE}} + F^{\mathrm{GCE}}\right) + F^{\mathrm{C}} \tag{10}$$

where F^{H} is the Hartree operator (i.e., the non-exchange part of the Hartree-Fock operator), F^{HFE} is the Hartree-Fock exchange operator, X is the fraction of Hartree-Fock (HF) exchange, F^{SE} is the Dirac-Slater local density functional for exchange, F^{GCE} is the gradient correction for the exchange functional, and F^{C} is the total correlation functional including both local and gradient-corrected parts. The functionals used here are mPW1PW91 [63–65], B1B95 [66–69], and mPW1B95 [54, 64, 68] in conjunction with the 6–31+G(d,p) basis set. We will refer in the rest of the paper to all methods as just HDFT methods even though, to be precise, whereas mPW1PW91 is a hybrid DFT, mPW1B95 and B1B95 are actually hybrid meta DFT methods.

In the SRP approach employed here, we parameterized the value of X in Eq. (10) to create potential energy surfaces that yield VTST/MT rate constants very close to the experimental ones. The HDFT methods obtained for different values of X are labeled by defining the gradient correlated exchanged functional used, followed by 1 to indicate a one-parameter method, followed by the correlation functional used, and finally by the value of X (given as a percent) separated by dash. For example, mPW1PW91–40.7 represents a hybrid density functional theory method based on modified Perdew-Wang (mPW) [64] gradient-corrected exchange functional and PW91 [63] gradient-corrected correlation functional with 40.7% HF exchange contribution [70]. The K methods (MPW1K, BB1K, and MPWB1K) developed by Truhlar and co-workers [54, 65, 69] were relabeled in this study, according to the convention above, as mPW1PW91–42.8, B1B95–42.0, and mPW1B95–44.0, respectively.

Computational details

All electronic structure calculations were carried out using *Gaussian*03 software [71]. The geometry optimizations

were performed using a tight convergence criteria and an ultrafine integration grid for numerical integrations. Restricted wave functions were used for closed-shell systems and unrestricted wave functions for open-shell systems.

Direct dynamics calculations are carried out with the GAUSSRATE [72] computer program, which interfaces the POLYRATE [73] and GAUSSIAN [71] programs. The partition functions were calculated assuming the rigid rotor-harmonic oscillator approximation. In calculating the electronic partition function of the hydroxyl radical, we included the $^2\prod_{1/2}$ electronic excited state with excitation energy of 140 cm^{-1}. For the generalized transition state, no low-lying electronically excited states were considered so the electronic partition function was the ground state multiplicity, which is 2. The symmetry factor, defined in Eq. (7), was calculated according to the general expression: [74–76]

$$\sigma = \frac{n^{GT}}{n^{HO} n^{CH_2F_2}} \frac{\sigma^{HO}\sigma^{CH_2F_2}}{\sigma^{GT}} \tag{11}$$

where n represents the number of optically active isomers for each species, and σ represents the rotational symmetry number for each species. The values for the generalized transition state are assumed to be the same as for the saddle point. In this case, $\sigma^{HO} = \sigma^{GT} = 1$ due to the $C_{\infty v}$ and C_1 symmetry of the HO and the saddle point, respectively, and $\sigma^{CH_2F_2} = 2$ due to the C_{2v} symmetry of CH_2F_2. Moreover, the reactants are achiral, so $n^{HO} = n^{CH_2F_2} = 1$, while there are two saddle points which are mirror image of each other, so that $n^{GT} = 2$, giving σ equal to 4.

The MEP in isoinertial coordinates was calculated by the Page-McIver method [77]. In all direct dynamics calculations, the coordinates were scaled to a reduced mass μ of 1 amu. A step size of 0.005 a_0 between gradient calculations was used, and a Hessian was calculated every 0.05 a_0 along the MEP. Calculations were carried out far enough along the reaction path to fully converge the tunneling calculations. The vibrational frequencies along the reaction path were evaluated using a set of redundant internal coordinates [78] that consists of six stretches, eleven nondegenerate bends, and three torsions. The choice of these redundant internal coordinates that were used in generalized, normal-mode, vibrational analyses, yielded in each case a reaction-path Hamiltonian with all frequencies real along MEP in the product region and close to the saddle point but not over the whole reactant region. To improve the generalized normal mode analysis along the MEP, in this work, a frequency cut-off option was used [79]. In this treatment, a cutoff value is used instead of the value determined from the generalized normal mode analysis if the later is smaller. In the present work, the frequency cutoff was set to the lowest positive frequency at the saddle point, which is around 20 cm^{-1} [1].

Results

The results of our calculations are presented in three tables and six figures. In Table 1, the energetic parameters for the title reaction calculated with different HDFT methods are presented. In this table, ΔE is the classical energy of reaction, ΔH_0 is the zero-point-inclusive energy of reaction, $V^{\ddagger}$ is the classical (i.e., zero-point-exclusive) barrier height, $\Delta H_0^{\ddagger}$ is the zero-point-inclusive barrier height, $E_a^{\ddagger}$ is Arrhenius activation energy at 298 K obtained on the basis of k^{TST}, $E_a^{V/T}$ is Arrhenius activation energy at 298 K obtained on the basis on $k^{CVT/SCT}$, $\Delta G_{298}^{\ddagger}$ is the conventional TST free energy of activation at 298 K, and $\omega^{\ddagger}$ is the imaginary frequency at the saddle point. The zero-point-inclusive barrier height, $\Delta H_0^{\ddagger}$, is calculated as:

$$\Delta H_0^{\ddagger} = V^{\ddagger} + \sum_{m=1}^{14} \frac{\hbar\omega_m^{\ddagger}}{2} - \sum_{n=1}^{9} \frac{\hbar\omega_n^{CH_2F_2}}{2} - \frac{\hbar\omega^{OH}}{2} \tag{12}$$

where $\omega_m^{\ddagger}$ is the frequency of the normal mode m of the saddle point, $\omega_n^{CH_2F_2}$ is the frequency of the normal mode n of CH_2F_2, and ω^{OH} is the hydroxyl normal mode frequency. The Arrhenius activation energies at 298 K, $E_a^{\ddagger}$ and $E_a^{V/T}$, are obtained by fitting k^{TST} and $k^{CVT/SCT}$ to an Arrhenius expression and are calculated as:

$$E_a^{\ddagger} = \frac{RT_1T_2}{T_2 - T_1} \ln \frac{k^{TST}(T_2)}{k^{TST}(T_1)} \tag{13}$$

and

$$E_a^{V/T} = \frac{RT_1T_2}{T_2 - T_1} \ln \frac{k^{CVT/SCT}(T_2)}{k^{CVT/SCT}(T_1)} \tag{14}$$

where T_1=293 K and T_2=303 K. In Table 2, selected geometric parameters of the saddle points calculated on different HDFT surfaces are presented.

The calculated rate constants as well as experimental ones (where available) in the temperature range 200–1,500 K are presented in Table 3 for all investigated functionals. Only $k^{CVT/SCT}$ are shown in this table; some other calculated rate

[1] The actual values used are 19.01, 20.98, and 20.98 cm^{-1} for X= 35.7, 40.7, and 42.8, respectively, using the mPW1PW91 functional, 19.78, 19.99, and 19.99 cm^{-1} for X=37.0, 42.0, and 44.0, respectively, using the B1B95 functional, and 20.00, 17.36, and 19.27 cm^{-1} for X=41.0, 44.0, and 46.0, respectively, using the mPW1B95 functional. For mPW1B95–41.0 calculations, the lowest positive frequency at the saddle point was slightly dependent of the way in which the molecular geometry was described in Gaussian so the value of 20.00 cm^{-1} was chosen rather than calculated. This value is close to the average of calculated values and close to the values obtained with the other functionals

Table 1 Energetic parameters for $OH+CH_2F_2 \rightarrow H_2O+CHF_2$ reaction[a]

HDFT Method	ΔE	ΔH_0	$V^{\ddagger}$	$\Delta H_0^{\ddagger}$	$E_a^{\ddagger}$	$E_a^{V/T}$	$\Delta G_{298}^{\ddagger}$	$\omega^{\ddagger}$
MPW1PW91–X/6–31+G(d,p)								
X=25.0	−15.3	−15.8	1.0	−0.1	0.3	n.c.[b]	5.0	439 i
X=35.7	−13.9	−14.3	3.9	2.0	2.4	3.3	7.0	1049 i
X=40.7	−13.2	−13.7	5.2	3.2	3.6	4.1	8.3	1311 i
X=42.8[c]	−13.0	−13.4	5.8	3.7	4.2	4.5	8.8	1407 i
B1B95–X/6–31+G(d,p)								
X=28.0	−15.7	−16.2	1.5	0.3	0.7	n.c.	5.5	453 i
X=37.0	−14.4	−14.9	3.8	2.0	2.4	3.3	7.0	959 i
X=42.0[d]	−13.8	−14.2	5.1	3.1	3.5	4.2	8.2	1228 i
X=44.0	−13.5	−14.0	5.7	3.6	4.0	4.5	8.6	1324 i
MPW1B95–X/6–31+G(d,p)								
X=31.0	−15.5	−15.9	1.3	−0.1	0.3	n.c.	4.9	561 i
X=41.0	−14.0	−14.5	4.0	2.0	2.5	3.2	7.1	1141 i
X=44.0[e]	−13.6	−14.1	4.8	2.8	3.2	3.8	7.7	1291 i
X=46.0	−13.4	−13.8	5.4	3.3	3.7	4.1	8.3	1385 i

[a] All values are in kcal mol^{-1} except the imaginary frequency that is in cm^{-1}
[b] n.c. denotes not calculated
[c] MPW1K
[d] BB1K
[e] MPWB1K

constants are given as Supplementary Material. The accuracy of the calculated rate constants using various HDFT methods was monitored by means of two statistical measures of the average deviation [80]. The mean unsigned percentage error (MUPE), defined as

$$MUPE = \left(\frac{1}{N} \sum_{i=1}^{N} \left| \frac{k_i^{calc} - k_i^{exp}}{k_i^{exp}} \right| \right) \times 100\% \quad (15)$$

and the logarithmically averaged percentage error (LAPE) defined as

$$LAPE = \left(10^{AUPD} - 1\right) \times 100\% \quad (16)$$

$$AUPD = \frac{1}{N} \sum_{i=1}^{N} \left| \log_{10} \frac{k_i^{calc}}{k_i^{exp}} \right| \quad (17)$$

were used. In these equations, k_i^{calc} represents the calculated rate constant at a certain temperature, k_i^{exp} represents the experimental rate constant at the same temperature, and N is the number of different temperatures over which the comparison is made. Although MUPE is very familiar and used more extensively, it does not give a balanced representation of the cases in which the calculated rate constants are underestimated. In this case, the percent error is limited to 100%. LAPE however treats evenly both

Table 2 Geometric parameters for the saddle point of $OH+CH_2F_2 \rightarrow H_2O+CHF_2$ reaction[a]

HDFT Method	$r_{C\cdots H}^{\ddagger}$	$r_{H\cdots O}^{\ddagger}$	$r_{C\cdots O}^{\ddagger}$	$\theta_{C\cdots H\cdots O}^{\ddagger}$
MPW1PW91–X/6–31+G(d,p)				
X=25.0	1.174	1.397	2.569	175.3
X=35.7	1.199	1.320	2.517	175.5
X=40.7	1.207	1.299	2.503	175.3
X=42.8	1.210	1.291	2.498	175.3
B1B95–X/6–31+G(d,p)				
X=28.0	1.176	1.394	2.569	176.0
X=37.0	1.196	1.329	2.524	175.8
X=42.0	1.204	1.306	2.508	175.6
X=44.0	1.207	1.298	2.503	175.4
MPW1B95–X/6–31+G(d,p)				
X=31.0	1.180	1.373	2.551	174.9
X=41.0	1.201	1.312	2.510	174.9
X=44.0	1.205	1.300	2.502	175.0
X=46.0	1.208	1.292	2.498	174.9

[a] All distances are in A, the angles are in degrees.

Table 3 Calculated $\left(k^{CVT/SCT}\right)$ and experimental rate constants (in $cm^3molecule^{-1}s^{-1}$) determined on various surfaces as well as the average errors

Temp	MPW1PW91–X/6–31+G(d,p)			B1B95–X/6–31+G(d,p)			MPW1B95–X/6–31+G(d,p)			exp
(K)	*X*=35.7	*X*=40.7	*X*=42.8	*X*=37.0	*X*=42.0	*X*=44.0	*X*=41.0	*X*=44.0	*X*=46.0	
200	4.9(−15)[a]	3.5(−16)	1.3(−16)	4.4(−15)	3.5(−16)	1.4(−16)	4.5(−15)	1.2(−15)	3.7(−16)	n.a.[b]
250	2.1(−14)	2.2(−15)	9.0(−16)	1.9(−14)	2.3(−15)	1.0(−15)	1.9(−14)	6.0(−15)	2.2(−15)	4.0(−15)
298	5.7(−14)	7.9(−15)	3.6(−15)	5.4(−14)	8.5(−15)	4.2(−15)	5.1(−14)	1.9(−14)	8.1(−15)	9.8(−15)
300	5.9(−14)	8.3(−15)	3.8(−15)	5.6(−14)	9.0(−15)	4.4(−15)	5.3(−14)	2.0(−14)	8.4(−15)	1.0(−14)
350	1.3(−13)	2.3(−14)	1.2(−14)	1.3(−13)	2.5(−14)	1.4(−14)	1.2(−13)	5.2(−14)	2.4(−14)	2.3(−14)
400	2.5(−13)	5.3(−14)	2.8(−14)	2.5(−13)	5.8(−14)	3.4(−14)	2.3(−13)	1.1(−13)	5.4(−14)	4.6(−14)
450	4.3(−13)	1.0(−13)	5.9(−14)	4.3(−13)	1.2(−13)	7.0(−14)	3.9(−13)	2.1(−13)	1.1(−13)	8.6(−14)
500	6.8(−13)	1.8(−13)	1.1(−13)	6.7(−13)	2.0(−13)	1.3(−13)	6.2(−13)	3.5(−13)	1.9(−13)	n.a.
600	1.4(−12)	4.6(−13)	3.0(−13)	1.4(−12)	5.1(−13)	3.5(−13)	1.3(−12)	8.2(−13)	4.8(−13)	n.a.
700	2.6(−12)	9.5(−13)	6.4(−13)	2.6(−12)	1.1(−12)	7.5(−13)	2.4(−12)	1.6(−12)	9.9(−13)	n.a.
800	4.2(−12)	1.7(−12)	1.2(−12)	4.2(−12)	1.9(−12)	1.4(−12)	3.9(−12)	2.8(−12)	1.8(−12)	n.a.
900	6.5(−12)	2.8(−12)	2.1(−12)	6.4(−12)	3.1(−12)	2.4(−12)	6.0(−12)	4.5(−12)	3.0(−12)	n.a.
1,000	9.3(−12)	4.4(−12)	3.2(−12)	9.3(−12)	4.8(−12)	3.8(−12)	8.7(−12)	6.8(−12)	4.6(−12)	n.a.
1,200	1.7(−11)	8.9(−12)	6.9(−12)	1.7(−11)	9.9(−12)	7.9(−12)	1.6(−11)	1.4(−11)	9.5(−12)	n.a.
1,500	3.6(−11)	2.1(−11)	1.7(−11)	3.6(−11)	2.3(−11)	1.9(−11)	3.4(−11)	3.0(−11)	2.2(−11)	n.a.
MUPE	430	31	53	409	36	45	375	102	32	
LAPE	429	46	149	407	50	104	374	95	45	

[a] $4.9(-15) \equiv 4.9 \times 10^{-15}$

[b] n.a. denotes not available.

underestimates and overestimates of the experimental rate constants and was used for the analysis of our results. MUPE and LUPE are also given in Table 3.

Figure 1 shows V_{MEP} and V_a^G along the reaction coordinate determined with the mPW1PW91–40.7, B1B95–42.0, and mPW1B95–46.0 functionals, respectively, and the 6–31+G(d,p) basis set[2]. In these figures, all reported energies are relative to the zero-point-exclusive energy of the reactants, which is considered the zero of energy. Figure 2 exhibits a two-dimensional representation of the MEPs calculated at the same levels of theory as Fig. 1, and insets for the saddle point and dynamical bottleneck regions. Figures 3, 4, and 5 show Arrhenius representations of the calculated rate constants obtained using the mPW1PW91, the B1B95, and the mPW1B95 functional, respectively, with different HF contributions. In these figures, the experimental values obtained from the fit of Clyne and Holt [7] are represented by ♢, the values obtained from the fit of Jeong and Kaufman [9] are represented by Δ, the values obtained from the fit of Talukdar et al. [11] are represented by □, the values obtained from the fit of Hsu and DeMore [13] are represented by ○, and the experimental values that were used in determining the accuracy of HDFT methods, as described below, are represented by ×. Finally, Fig. 6 shows LAPE and MUPE in calculated rate constants for the title reaction versus the percentage contribution of HF exchange for all three functionals investigated in this study.

[2] The vibrationally adiabatic ground-state potential energy curves obtained on mPW1PW91–40.7 and B1B95–42.0 surfaces have an unphysical bump on the reactant side that is due to numerical errors in the calculation of the generalized normal modes. This result does not however change at all the calculated rate constants.

Analysis and discussion

Parameterized HDFT methods

The goal of this study is to determine HDFT methods that provide accurate calculated rate constants for the title reaction using VTST/MT and to describe the dynamically significant region of the PES generated with these methods. For each of the three functionals investigated here, we initially carried out direct dynamics calculations using the HDFT methods (mPW1PW91–35.7, B1B95–37.0, and mPW1B95–41.0) that give accurate rate constants for the $HO+CH_3F$ reaction [4]. We performed a second set of dynamics calculations using the functionals designed for kinetics by Truhlar and coworkers (i.e., the K methods: MPW1K, BB1K, and MPWB1K, respectively).

For each functional, we carried out a third set of dynamics calculations using three HDFT methods that were chosen, as described below, to assure that at least one HDFT method gives accurate dynamics results. The procedure was based on the rate constant at only one temperature, and we choose the temperature of 340 K to make the comparison between the calculated rate constants

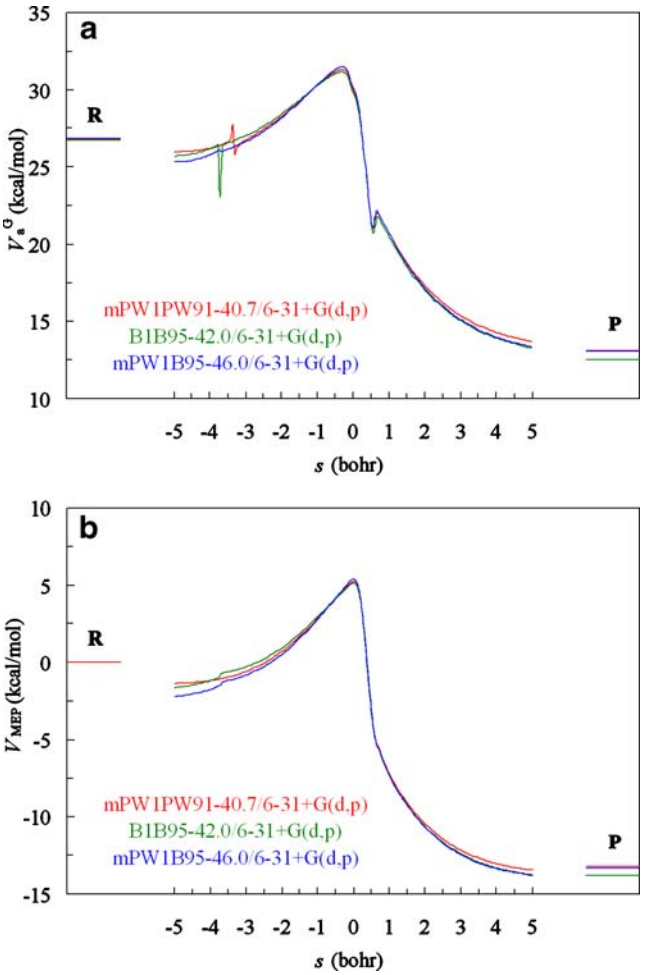

Fig. 1 Reaction path profiles ($-5.0\ a_0<s<+5.0\ a_0$) for $OH+CH_2F_2 \rightarrow H_2O+CHF_2$ reaction determined on three HDFT surfaces that provide accurate calculated rate constants. **a** The vibrationally adiabatic ground-state potential energy curves, V_a^G, and **b** the potential energy curves along the minimum energy path, V_{MEP}. R represents the reactant state and P represents the product state

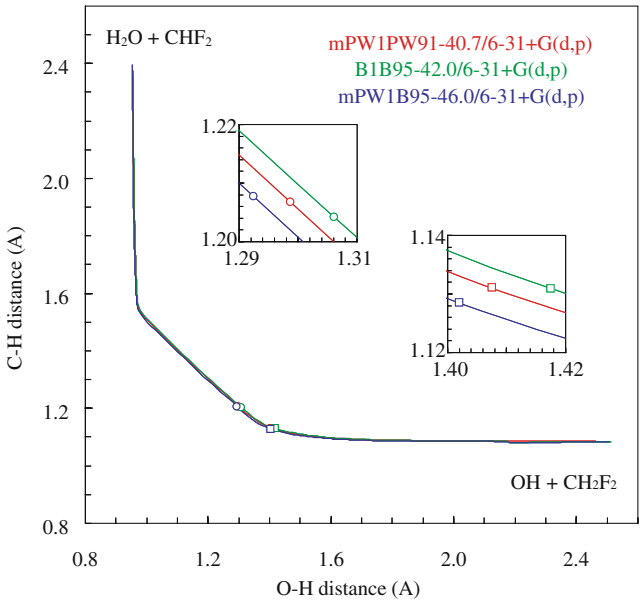

Fig. 2 A two-dimensional representation of the reaction paths ($-5.0\ a_0<s<+5.0\ a_0$) determined on three HDFT surfaces that provide accurate calculated rate constants. The *circles* represent the saddle points, $s=0$, the *squares* represent the dynamical bottlenecks at 298 K, $s_*^{CVT}(298)$

and the experimental one that was determined from the four experimental fits. The temperature of 340 K was chosen because this value is in the middle of the temperature range where all four fits are available. We defined a target experimental rate constant value of 1.98×10^{-14} $cm^3molecule^{-1}s^{-1}$ at 340 K that was obtained as an average of the four rate constants (1.54×10^{-14}, 2.41×10^{-14}, 2.08×10^{-14}, and 1.87×10^{-14} $cm^3molecule^{-1}s^{-1}$, respectively) obtained from the four available experimental fits [7, 9, 11, 13]. On the basis of the results from the first two sets of dynamics calculations, assuming a linear relationship between $\log k^{CVT/SCT}$ versus the HF exchange contribution (X), we determined two new HDFT methods that would give rate constants very close to our target: mPW1PW91–40.7 and mPW1B95–46.0. This determination was done through interpolation for the mPW1PW91 functional and through extrapolation for the mPW1B95 functional. After carrying out the dynamics calculations, we indeed determined that the mPW1PW91–40.7 and mPW1B95–46.0 methods provide calculated rate constants within an acceptable range (15%) of the target experimental rate constant at 340 K. For the B1B95 functional, the B1B95–42.0 method already give a rate constant close to the target value at 340 K so the third method, B1B95–44.0, was chosen such to have a larger X value than the accurate method.

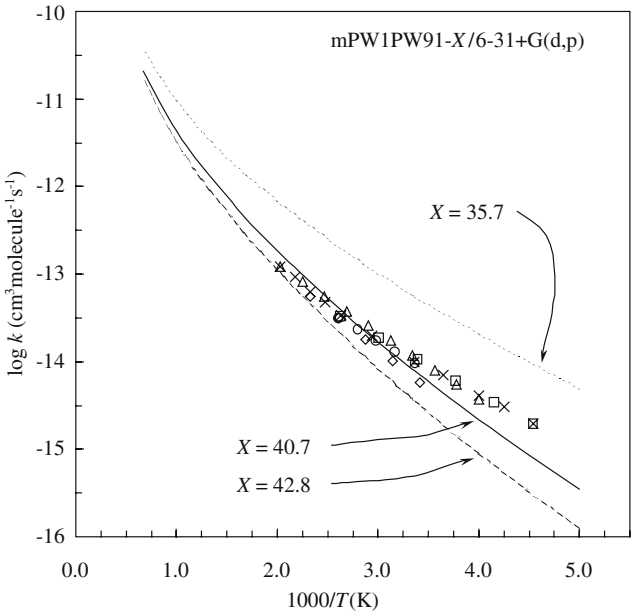

Fig. 3 Arrhenius plot of CVT/SCT rate constants calculated on mPW1PW91–*X*/6–31+G(d,p) surfaces compared with experimental results

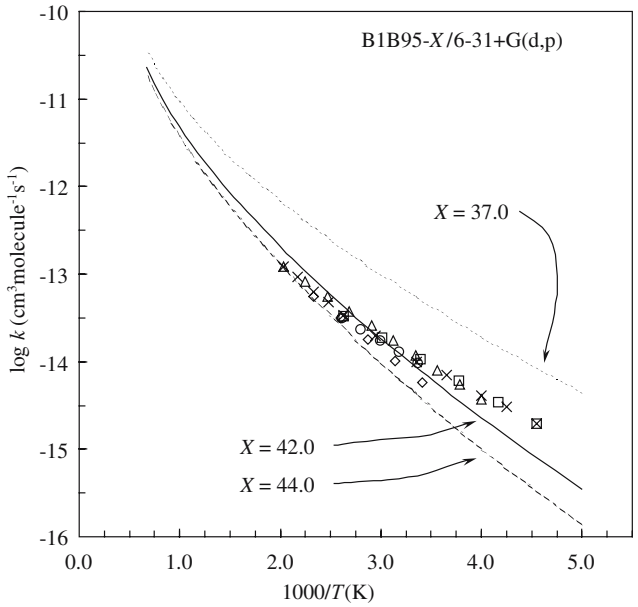

Fig. 4 Arrhenius plot of CVT/SCT rate constants calculated on B1B95–*X*/6–31+G(d,p) surfaces compared with experimental results

In Tables 1 and 2, we also present results obtained for the generic mPW1PW91, B1B95, and mPW1B95 methods (with X=25.0, X=28.0, and X=31.0, respectively). These results were determined only from the properties of the saddle point; no dynamics calculations were carried out using these methods.

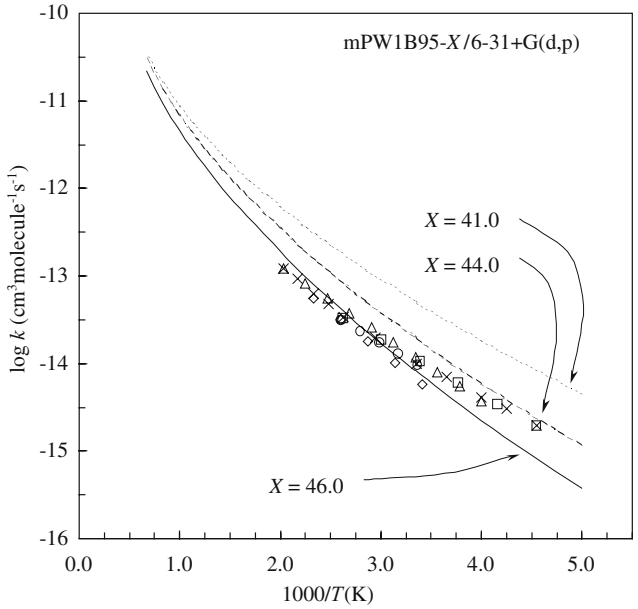

Fig. 5 Arrhenius plot of CVT/SCT rate constants calculated on mPW1B95–*X*/6–31+G(d,p) surfaces compared with experimental results

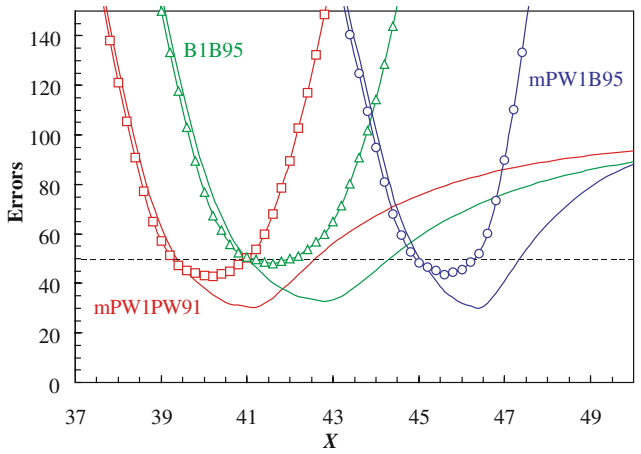

Fig. 6 Average percentage error of all the three methods as a function of the HF exchange contribution to the exchange-correlation functional. LAPE are the *curves with symbols* (*squares* for mPW1PW91-*X*, *triangles* for B1B95-*X*, and *circles* for mPW1B95-*X*), MUPE are the *curves without symbols*

Calculated rate constants

In previous studies of $OH+CH_3F$ and $OH+CHF_3$ hydrogen abstraction reactions [4, 5], the tunneling contributions were calculated using both the SCT approximation and version 4 of the large-curvature tunneling (LCT) approximation [80, 81–83], where the LCT results include tunneling into vibrationally excited states. On all investigated surfaces, both reactions were dominated by small-curvature tunneling so one could assume that the same were true for the $OH+CH_2F_2$ reaction. We therefore calculated the tunneling contributions for the title reaction using only the SCT approximation.

The CVT/SCT rate constants calculated on all investigated HDFT surfaces over the temperature range 200–1500 K are given in Table 3. The errors are also given in this table, but they are calculated over the smaller temperature range, where experimental data is available, as described below. The four available experimental data fits (given by Eqs. 2–5) are over the 220–492 K temperature range. The analysis of the accuracy of an HDFT method was carried out using a set of eleven temperatures spread over this temperature range. Six of these eleven temperatures, 220, 250, 298, 380, 429, and 492 K, are end points (or close to end points) of the four experimental fits, and the other five temperatures, 235, 274, 340, 404, and 460, are medians (or close to medians) of the five temperature intervals defined by the original six points. For four of these temperatures (220, 235, 460, and 492 K) there is only one experimental fit available, and the experimental rate constants at these temperatures were obtained from that fit only. For four temperatures (250, 274, 404, and 429 K) there are two fits available, and for the other three temperatures (298, 340, and 380 K) all four fits are

available, and the experimental rate constants at these seven temperatures were obtained as the average of the values obtained from each available fit.

For each one of these eleven temperatures and for each functional, we fitted the three calculated $\log k^{CVT/SCT}$ versus the HF exchange contribution (X) representation to a second order polynomial. For each functional, this fit was then used to calculate a rate constant for each value of X within a certain range. (The quadratic polynomial fits are provided as Supplementary Material.) Knowing $\log k^{CVT/SCT}$ as a function of the X value, one can calculate MUPE and LAPE as a function of the X value. LAPE and MUPE versus X representations for all three examined functionals are given in Fig. 6. This figure illustrates the X value range that one should use to obtain calculated rate constants (using VTST/MT dynamics calculations on a PES obtained using HDFT method in conjunction with the 6–31+G(d,p) basis set) that are, on average, within a certain desired accuracy with respect to the experimental values.

As in the previous studies [4, 5], in interpreting these results (and in calculating rate constants that are not available experimentally), it is considered acceptable if the average error in the calculated rate constants is less than 50%. It is of course preferred to obtain errors much smaller than this, but one should take into account that direct dynamics results using VTST/MT give rate constants that are, on average, within 25–30% of the experimental or the accurate quantum mechanical dynamics rate constants [80, 84, 85]. Our dynamics calculations also include additional approximations (such as not including the anharmonicity or not using scaled vibrational frequencies in calculating vibrational partition functions) that may increase (although they can also decrease) the inaccuracy of the calculated rate constants, so accepting 50% errors in calculated rate constants is reasonable. (For kinetic isotope effects calculations, the errors would be, however, larger than 50% if the rate constants for isotopic substituted reactants were on opposite directions of the experimental values.) Our analysis gives the range of X that provides calculated rate constants that are within 50% of the experimental data. These are 39.2–41.0 using mPW1PW91, 41.0–42.2 using B1B95, and 44.9–46.3 using mPW1B95 functional, respectively. The optimal values of X are 40.1 for mPW1PW91, 41.6 for B1B95, and 45.7 for mPW1B95 functional, respectively. The lowest LAPE obtained with either one of these HDFT methods (with optimal X values) is around 45%. In comparison, for the HO+CH_3F reaction we obtained average errors as low as 5% [4], while for the HO+CHF_3 reaction the smallest errors were around 35% [5]. The higher average errors obtained here for the HO+CH_2F_2 reaction is due to the fact that no PES employed here accurately reproduce the experimental rate constants both at very low temperatures and at high temperatures. From Figs. 3, 4 and 5, it is noticeable that HDFT methods with higher X reproduce better the experimental results at higher temperatures (than at lower temperatures) while HDFT methods with lower X reproduce better the experimental results at lower temperatures (than at higher temperatures). It is also interesting to point out that among the K methods, BB1K give better results (LAPE=50, at the edge of the range of acceptable errors) than MPWB1K (LAPE=95), which in turn is better than MPW1K (LAPE=149).

Our direct dynamics calculations show that the tunneling contributions are not very significant but they can be important at very low temperatures. At 298 K, among the three HDFT methods that give accurate rate constants, the transmission coefficients are relatively small. The transmission coefficient is the highest for the mPW1B95–46.0 functional (κ^{SCT}=2.08), then the mPW1PW91–40.7 functional (κ^{SCT}=1.86), and the smallest for the B1B95–42.0 functional (κ^{SCT}=1.64). The tunneling contributions are slightly more significant at lower temperatures. Although the multidimensional tunneling calculations employed here require information along the whole reaction path, the results are consistent with one's expectation based on the saddle point properties. The tunneling is expected to be more significant on the PES with a higher classical barrier height and a higher imaginary frequency at the saddle point, and we indeed observe this trend. Tunneling is also more significant on the PES with a smaller perpendicular looseness, a quantity that will be defined in Section Saddle point and dynamical bottleneck properties.

As discussed in more detail in the study of the HO+CH_3F reaction, [4] the use of scaled vibrational frequencies or the inclusion of anharmonicity effects will increase the calculated rate constants leading to a slightly lower optimal value of the HF exchange contribution. The differences were however found to be within our reliability range of 50%, and we expect the same behavior for the title reaction.

One possible use of the present kind of study is predicting the rate constant outside the range where is has been measured. For example, the three SRP potentials presented here predict k at 200 K to be in the range 3.5–3.7×10^{-16} $cm^3molecule^{-1}s^{-1}$, but since the rates are underestimated at 250–300 K, this would be a predicted lower bound; and k at 1500 K is predicted to be in the range 2.1–2.3×10^{-11} $cm^3molecule^{-1}s^{-1}$ but since the rates are overestimated at 350–700 K, this should be interpreted as an approximate upper bound.

Reaction energetics

One of the advantages of using HDFT methods in creating PES for dynamics calculations is that the energetics in the saddle point region is very dependent on the HF exchange contribution. Inspecting the results in Table 1, one obvious

observation is that the calculated classical barrier height increases with the increase in the HF exchange contribution to the exchange-correlation energy. The generic HDFT methods (with lower values of X) give small barrier heights, and the HDFT methods designed for kinetics (i.e., the K methods) give, for the title reaction, good estimates of the classical barrier height, with calculated values of 5.8, 5.1, and 4.8 kcal mol^{-1} for MPW1K, BB1K, and MPWB1K, respectively. The HF exchange contribution that one uses to get a certain barrier height depends on the choice of gradient-corrected exchange and correlation functional used. To obtain a barrier height of a certain value, one should use higher HF exchange contribution for the mPW1B95 functional than for the B1B95 functional or the mPW1PW91 functional. For example, the mPW1PW91–35.7, B1B95–37.0, and mPW1B95–41.0 methods give classical barrier heights of 3.9, 3.8, and 4.0 kcal mol^{-1}, respectively, (i.e., very close barrier heights) by using different (i.e., increasing) HF exchange contributions.

To find the best estimate of the classical barrier height, we investigated in more detail the HDFT surfaces that give accurate rate constants in conjunction with VTST/MT dynamics calculations. To be more precise, based on the range of X values giving accurate rate constants, one can determine a range of barrier height values. To find this range, for each of the three functionals investigated, we fitted the calculated barrier heights versus X to a quadratic form and found, on the basis of the fit and knowing the limits of X that give calculated rate constants within the acceptable accuracy range of 50%, classical barrier heights of 4.84–5.32 kcal mol^{-1} for the mPW1PW91 functional, 4.87–5.19 kcal mol^{-1} for the B1B95 functional, and 5.08–5.46 kcal mol^{-1} for the mPW1B95 functional. Combining the results for all three functionals examined here, we propose a best estimate range of 5.0–5.3 kcal mol^{-1} for the title reaction. (The most accurate rate constants are obtained for surfaces with an average classical barrier height of 5.14 kcal mol^{-1}.) This classical barrier height estimate is higher than the modified G2 [36] value of 4.0 kcal mol^{-1} determined by Korchowiec et al. [23], but is essentially the same as the CCSD(T)//MP2/cc-pVTZ value of 5.1 used by Espinosa-Garcia and coworkers [27].

Saddle point and dynamical bottleneck properties

The results in Table 2 show that the HDFT methods with smaller X values give early transition states characterized by shorter C···H distances and longer H···O distances, whereas HDFT methods with bigger X values give late (or later) transition states. We also investigated the sum of the making $\left(r^{\ddagger}_{\mathrm{H\cdots O}}\right)$ and breaking $\left(r^{\ddagger}_{\mathrm{C\cdots H}}\right)$ bond distances, called perpendicular looseness, which is a measure of the looseness of the structure in a direction perpendicular to the reaction coordinate. As in the previous studies [4, 5], we found that the transition state gets looser as the HF exchange contribution decreases. When only the three HDFT methods that give accurate calculated rate constants are compared, the mPW1B95–46.0 method gives a slightly tighter transition state $\left(r^{\ddagger}_{\mathrm{C\cdots H}} + r^{\ddagger}_{\mathrm{H\cdots O}} = 2.500\,\mathrm{A}\right)$ while B1B95–42.0 method gives a slightly looser transition state $\left(r^{\ddagger}_{\mathrm{C\cdots H}} + r^{\ddagger}_{\mathrm{H\cdots O}} = 2.510\,\mathrm{A}\right)$. This is also seen in Fig. 2 where the reactions paths and the saddle point locations (in inset) are represented. The difference is mainly due to a longer H···O distance at the transition state. Note also that the C···H···O angle is less than 180 degrees so $r^{\ddagger}_{\mathrm{C\cdots O}} < r^{\ddagger}_{\mathrm{C\cdots H}} + r^{\ddagger}_{\mathrm{H\cdots O}}$. For the HDFT methods used in this study and the 6–31+G(d,p) basis set, the C···H···O angle is around 175 degrees.

The imaginary frequency at the saddle point can be seen as a measure of the thickness of the barrier. A high imaginary frequency indicates a large negative force constant for the reaction coordinate mode at the saddle point and, therefore, at least near the barrier top, a thin barrier. All other factors being equal, a thinner barrier gives increased tunneling probabilities in dynamics calculations. Among the HDFT methods that give the same (or very similar) rate constants, the mPW1B95 functional gives the narrowest barrier (highest value for the imaginary frequency and the smallest perpendicular looseness) and the B1B95 functional gives the widest barrier. Not surprisingly, the calculated transmission coefficients are calculated to be higher for the mPW1B95 functional. Based on our results, the best estimate of the imaginary frequency at the saddle point is 1,290i cm^{-1}.

The dynamical bottleneck at 298 K is located at s=−0.282 a_0, s=−0.302 a_0, and s=−0.273 a_0 using mPW1PW91–40.7, B1B95–42.0, and mPW1B95–46.0 method, respectively. At the dynamical bottleneck at 298 K, the C···H distance is around 1.13 A, and the O···H distance is around 1.41 A (Fig. 2 inset). The location of the dynamical bottleneck, quite far away from the saddle point, illustrates large variational effects for this reaction. This leads also to significant differences between the calculated k^{CVT} and k^{TST} (see the rate constants given as Supplementary Material). The temperature dependence of the dynamical bottleneck location is not very significant. For example, on the mPW1B95–46.0 surface, the dynamical bottleneck is located at s=−0.282 a_0 at 200 K, at s=−0.258 a_0 at 500 K, and at s=−0.244 a_0 at 1000 K.

HDFT methods for hydrogen abstraction from fluoromethanes by hydroxyl radical

The present study is an extension of our previous studies on the OH+CH_3F and OH+CHF_3 reactions [4, 5]. We were interested in determining if the HDFT-SRP methods

developed for a reaction can be easily transferable (i.e., applicable) to another, similar reaction without significantly decreasing its accuracy. This is equivalent to determining the accuracy of an HDFT method for more then one reaction so, to quantify the accuracy of an HDFT-SRP method for all three hydrogen abstraction reactions from fluoromethanes ($OH+CH_3F$, $OH+CH_2F_2$, and $OH+CHF_3$), we defined an average LAPE (ALAPE) that is obtained as the average of LAPE for each reaction. Although the LAPE for each reaction was determined over different temperature ranges, this was not considered when determining ALAPE. Considering all three hydrogen abstraction reactions, the lowest ALAPE for a HDFT method is around 150–160%. This result shows that any HDFT-SRP method can provide very accurate results for only one reaction and not for all three hydrogen abstraction reactions for fluoromethanes.

To further analyze the results, we considered an accepted ALAPE of less than 200% (i.e., calculated rate constants are different from the experimental ones, on average, by a factor of 3). This error would be very significant when calculating certain properties like the barrier height or the energy of reaction but is not excessively high when calculating rate constants. (For example, a 200% error in the rate constant at 300 K is a result of an error in the calculated classical barrier height of about 0.6 kcal mol^{-1}, which is about 10% of the calculated value for the barrier height for this reaction.) Typical ab initio and hybrid density functional theory methods, with computational costs similar to the methods used in the current study, will most likely give much higher errors, that can be as high as few orders of magnitude.

Our analysis gives the range of X that provides calculated rate constants that are within 200% of the experimental data, when averaged for all three reactions (ALAPE<200). These X ranges are 35.3–38.8 using mPW1PW91, 36.4–40.1 using B1B95, and 39.7–43.7 using mPW1B95 functional, respectively. The optimal values of X are 36.9 for mPW1PW91, 38.1 for B1B95, and 41.5 for mPW1B95 functional, respectively. It is also interesting to point out that among the K methods, MPWB1K give better results (ALAPE=213) than BB1K (ALAPE=373), which in turn is better than MPW1K (ALAPE=790).

Summary

HDFT methods are very attractive methods for use in chemical dynamics studies because they are accurate and affordable and because they are quite flexible in the choice of exchange and correlation functional that one uses. Our interest is in identifying HDFT methods that can be used for accurately investigating chemical dynamics of important environmental and atmospheric processes.

In this work, we have developed potential energy surfaces for the $OH+CH_2F_2 \rightarrow H_2O+CHF_2$ reaction based on hybrid density functional theory methods with a specific reaction parameter. These new HDFT methods, in conjunction with the 6–31+G(d,p) basis set, are used in calculating dynamic properties on single-level, accurate PESs without the use of dual-level dynamics. We carried out direct dynamics calculations on these surfaces using variational transition state theory with multidimensional tunneling contributions between 200 and 1,500 K. We determined three HDFT surfaces that give dynamics results that are in excellent agreement with available experimental data. The specific-reaction-parameter surfaces that give accurate calculated rate constants have an average classical barrier height of 5.14 kcal mol^{-1}, which is our best estimate for this reaction, although, since our temperature dependence is consistently higher than the experimental one, our barrier height might be too high as well.

The optimal HF exchange contributions obtained in this study are higher than the values obtained for the $OH+CH_3F$ and $OH+CHF_3$ reactions [4, 5]. It was found that no HDFT method gives very accurate results for all hydrogen abstraction reactions from fluoromethanes but the investigated HDFT-SRP methods give however much better results than the generic HDFT methods. It is established that mPW1PW91–36.9, B1B95–38.1, and mPW1B95–41.5 methods in conjunction with the 6–31+G(d,p) basis set should provide quite accurate results for the three hydrogen abstraction reactions from fluoromethanes.

Acknowledgments The authors thank Professor Donald G. Truhlar for providing POLYRATE and GAUSSRATE computer programs, and Dr. Hai Lin for providing us the modifications to the POLYRATE software that allow calculations with frequency cutoff option. This research was supported in part by Tennessee Technological University through a Faculty Research Initiation Program.

References

1. Brasseur GP, Orlando JJ, Tyndall GS (1999) Atmospheric Chemistry and Global Change. Oxford University Press, New York, NY
2. Elkins JW (1999) In: Alexander DE, Fairbridge, RW (eds) Encyclopedia of Environmental Science. Kluwer, Boston, MA, pp 78–80
3. Mikel SE, Albu TV (2006) J Und Chem Res 5:75–81
4. Albu TV, Swaminathan S (2006) J Phys Chem A 110:7663–7671
5. Albu TV, Swaminathan S (2007) Theor Chem Acc 117:383–395
6. Howard CJ, Evenson KM (1976) J Chem Phys 64:197–202
7. Clyne MAA, Holt PM (1979) J Chem Soc Faraday Trans 75:582–591
8. Nip WS, Singleton DL, Overend R, Paraskevopoulos G (1979) J Phys Chem 83:2440–2443
9. Jeong KM, Kaufman F (1982) J Phys Chem 86:1808–1815
10. Bera RK, Hanrahan RJ (1988) Radiat Phys Chem 32:579–584

11. Talukdar R, Mellouki A, Gierczak T, Burkholder JB, McKeen SA, Ravishankara AR (1991) J Phys Chem 95:5815–5821
12. Schmoltner AM, Talukdar RK, Warren RF, Mellouki A, Goldfarb L, Gierczak T, McKeen SA, Ravishankara AR (1993) J Phys Chem 97:8976–8982
13. Hsu KJ, DeMore WB (1995) J Phys Chem 99:1235–1244
14. Szilagyi I, Dobe S, Berces T (2000) React Kinet Catal Lett 70:319–324
15. Atkinson R (1986) Chem Rev 86:69–201
16. Atkinson R, Baulch DL, Cox RA, Hampson RF Jr, Kerr JA, Rossi MJ, Troe J (1997) J Phys Chem Ref Data 26:521–1013
17. DeMore WB (2005) J Photoch Photobio A 176:129–135
18. Jeong KM, Kaufman F (1982) J Phys Chem 86:1816–1821
19. Cohen N, Benson SW (1987) J Phys Chem 91:162–170
20. Bottoni A, Poggi G, Emmi SS (1993) Theochem 297:299–309
21. Jursic BS (1996) Chem Phys Lett 256:603–608
22. Schwartz M, Marshall P, Berry RJ, Ehlers CJ, Petersson GA (1998) J Phys Chem A 102:10074–10081
23. Korchowiec J, Kawahara S-i, Matsumura K, Uchimaru T, Sugie M (1999) J Phys Chem A 103:3548–3553
24. Chandra AK, Uchimaru T, Sugie M, Sekiya A (2000) Chem Phys Lett 318:69–74
25. Louis F, Gonzalez CA, Huie RE, Kurylo MJ (2000) J Phys Chem A 104:8773–8778
26. El-Taher S (2001) Int J Quantum Chem 84:426–440
27. Gonzalez-Lafont A, Lluch JM, Espinosa-Garcia J (2001) J Phys Chem A 105:10553–10561
28. Korchowiec J (2002) J Phys Org Chem 15:524–528
29. Møller C, Plesset MS (1934) Phys Rev 46:618
30. Schlegel HB (1986) J Chem Phys 84:4530–4534
31. Sosa C, Schlegel HB (1986) Int J Quantum Chem 29:1001–1015
32. Schlegel HB (1988) J Phys Chem 92:3075–3078
33. Wigner E (1932) Z Phys Chem B 19:203
34. Curtiss LA, Raghavachari K, Trucks GW, Pople JA (1991) J Chem Phys 94:7221–7230
35. Curtiss LA, Raghavachari K, Pople JA (1993) J Chem Phys 98:1293–1298
36. Mebel AM, Morokuma K, Lin MC (1995) J Chem Phys 103:7414–7421
37. Garrett BC, Truhlar DG (1979) J Phys Chem 83:2921–2926
38. Hu WP, Liu YP, Truhlar DG (1994) J Chem Soc Faraday Trans 90:1715–1725
39. Corchado JC, Coitino EL, Chuang Y-Y, Fast PL, Truhlar DG (1998) J Phys Chem A 102:2424–2438
40. Chuang Y-Y, Corchado JC, Truhlar DG (1999) J Phys Chem A 103:1140–1149
41. Albu TV, Corchado JC, Truhlar DG (2001) J Phys Chem A 105:8465–8487
42. Garrett BC, Truhlar DG (1979) J Chem Phys 70:1593–1598
43. Truhlar DG, Garrett BC (1980) Acc Chem Res 13:440–448
44. Garrett BC, Truhlar DG (1984) J Chem Phys 81:309–317
45. Truhlar DG, Garrett BC (1984) Ann Rev Phys Chem 35:159–189
46. Truhlar DG, Garrett BC, Hipes PG, Kuppermann A (1984) J Chem Phys 81:3542–3545
47. Truhlar DG, Isaacson AD, Garrett BC (1985) In: Baer M (ed) Theory of Chemical Reaction Dynamics, Vol. 4. CRC Press, Boca Raton, FL, pp 65–137
48. Kreevoy MM, Truhlar DG (1986) In: Bernasconi CF (ed) Investigation of Rates and Mechanisms of Reactions, Vol. 6. Wiley, New York, pp 13–95
49. Tucker SC, Truhlar DG (1989) In: Bertran J, Csizmadia IG (eds) New Theoretical Concepts Understanding Organic Reactions, Vol. 267. Kluwer, Dordrecht, pp 291–346
50. Liu YP, Lynch GC, Truong TN, Lu DH, Truhlar DG, Garrett BC (1993) J Am Chem Soc 115:2408–2415
51. Truhlar DG, Garrett BC, Klippenstein SJ (1996) J Phys Chem 100:12771–12800
52. Garrett BC, Truhlar DG (2005) In: Dykstra CE, Frenking G, Kim K, Scuseria G (eds) Theory and Applications of Computational Chemistry: The First Forty Years. Elsevier, Amsterdam, pp 67–87
53. Coote ML (2004) J Phys Chem A 108:3865–3872
54. Zhao Y, Truhlar DG (2004) J Phys Chem A 108:6908–6918
55. Andersson S, Gruening M (2004) J Phys Chem A 108:7621–7636
56. Zhao Y, Truhlar DG (2005) J Phys Chem A 109:5656–5667
57. Gonzalez-Lafont A, Truong TN, Truhlar DG (1991) J Phys Chem 95:4618–4627
58. Pu J, Truhlar DG (2002) J Chem Phys 116:1468–1478
59. Truhlar DG, Kuppermann A (1971) J Am Chem Soc 93:1840–1851
60. Garrett BC, Truhlar DG (1979) J Phys Chem 83:1915–1924
61. Lin H, Zhao Y, Ellingson BA, Pu J, Truhlar DG (2005) J Am Chem Soc 127:2830–2831
62. Lu D-H, Truong TN, Melissas VS, Lynch GC, Liu Y-P, Garrett BC, Steckler R, Isaacson AD, Rai SN, Hancock GC, Lauderdale JG, Joseph T, Truhlar DG (1992) Comput Phys Commun 71:235–262
63. Perdew JP, Chevary JA, Vosko SH, Jackson KA, Pederson MR, Singh DJ, Fiolhais C (1992) Phys Rev B 46:6671–6687
64. Adamo C, Barone V (1998) J Chem Phys 108:664–675
65. Lynch BJ, Fast PL, Harris M, Truhlar DG (2000) J Phys Chem A 104:4811–4815
66. Becke AD (1988) Phys Rev A 38:3098–3100
67. Becke AD (1993) J Chem Phys 98:5648–5652
68. Becke AD (1996) J Chem Phys 104:1040–1046
69. Zhao Y, Lynch BJ, Truhlar DG (2004) J Phys Chem A 108:2715–2719
70. The keywords to carry out mPW1PW91–40.7 calculations in Gaussian03 are mPWPW91/6–31+G(d,p) and IOP(3/76=0593004070). The keywords to carry out B1B95–42.0 calculations in Gaussian03 are BB95/6–31+G(d,p) and IOP(3/76=0580004200). The keywords to carry out mPW1B95–46.0 calculations in Gaussian03 are mPWB95/6–31+G(d,p) and IOP(3/76=0540004600)
71. Frisch MJ, Trucks GW, Schlegel HB, Scuseria GE, Robb MA, Cheeseman JR, Montgomery JA, Vreven T, Kudin KN, Burant JC, Millam JM, Iyengar SS, Tomasi J, Barone V, Mennucci B, Cossi M, Scalmani G, Rega N, Petersson GA, Nakatsuji H, Hada M, Ehara M, Toyota K, Fukuda R, Hasegawa J, Ishida M, Nakajima T, Honda Y, Kitao O, Nakai H, Klene M, Li X, Knox JE, Hratchian HP, Cross JB, Adamo C, Jaramillo J, Gomperts R, Stratmann RE, Yazyev O, Austin AJ, Cammi R, Pomelli C, Ochterski JW, Ayala PY, Morokuma K, Voth GA, Salvador P, Dannenberg JJ, Zakrzewski VG, Dapprich S, Daniels AD, Strain MC, Farkas O, Malick DK, Rabuck AD, Raghavachari K, Foresman JB, Ortiz JV, Cui Q, Baboul AG, Clifford S, Cioslowski J, Stefanov BB, Liu G, Liashenko A, Piskorz P, Komaromi I, Martin RL, Fox DJ, Keith T, Al-Laham MA, Peng CY, Nanayakkara A, Challacombe M, Gill PMW, Johnson B, Chen W, Wong MW, Gonzalez C, Pople JA (2003) Gaussian 03, Revision B.02. Gaussian, Inc, Pittsburgh PA
72. Corchado JC, Chuang Y-Y, Coitiño EL, Truhlar DG (2003) GAUSSRATE 9.1. University of Minnesota, Minneapolis, MN
73. Corchado JC, Chuang Y-Y, Fast PL, Villà J, Hu W-P, Liu Y-P, Lynch GC, Nguyen KA, Jackels CF, Melissas VS, Lynch BJ, Rossi I, Coitiño EL, Fernandez-Ramos A, Pu J, Albu TV, Steckler R, Garrett BC, Isaacson AD, Truhlar DG (2003) POLYRATE 9.1. University of Minnesota, Minneapolis, MN
74. Pechukas P (1976) J Chem Phys 64:1516–1521
75. Pollak E, Pechukas P (1978) J Am Chem Soc 100:2984–2991
76. Bell RL, Truong TN (1994) J Chem Phys 101:10442–10451
77. Page M, McIver JW Jr (1988) J Chem Phys 88:922–935
78. Chuang Y-Y, Truhlar DG (1998) J Phys Chem A 102:242–247

79. Lin H, Pu J, Albu TV, Truhlar DG (2004) J Phys Chem A 108:4112–4124
80. Allison TC, Truhlar DG (1998) In: Thompson DL (ed) Modern Methods for Multidimensional Dynamics Computations in Chemistry. World Scientific, Singapore, pp 618–712
81. Liu YP, Lu DH, Gonzalez-Lafont A, Truhlar DG, Garrett BC (1993) J Am Chem Soc 115:7806–7817
82. Truong TN, Lu D-h, Lynch GC, Liu Y-P, Melissas VS, Steward JJP, Steckler R, Garrett BC, Isaacson AD, Gonzalez-Lafont A, Rai SN, Hancock GC, Joseph T, Truhlar DG (1993) Comput Phys Commun 75:143–159
83. Fernandez-Ramos A, Truhlar DG (2001) J Chem Phys 114:1491–1496
84. Pu J, Corchado JC, Truhlar DG (2001) J Chem Phys 115:6266–6267
85. Pu J, Truhlar DG (2002) J Chem Phys 117:1479–1481